Journal of Membrane Science 650 (2022) 120421

Contents lists available at ScienceDirect

Journal of Membrane Science

journal homepage: www.elsevier.com/locate/memsci

H_2O-enhanced CO_2 transport through a proton conducting ceramic- molten carbonate dual-phase membrane

Kangkang Zhang, Shichen Sun, Nansheng Xu, Kevin Huang [*]

Department of Mechanical Engineering, University of South Carolina, Columbia, SC, 29201, USA

ABSTRACT

High-temperature membranes for CO_2 transport and separation has attracted significant interest from academia and industries due to their potential to mitigate the emissions of CO_2 and ultimately global warming/climate change. In this study, we report a dual-phase CO_2 membrane fabricated from a porous proton conducting $BaZr_{0.8}Y_{0.2}O_{3-\delta}$ (BZY) matrix and eutectic mixture of Li_2CO_3–Na_2CO_3 (denoted as MC). The membrane exhibits a high CO_2 permeation flux density in the range of 550–750 °C in both dry and wet conditions. Through microstructural optimization, a CO_2 flux density as high as 0.34 $mL \cdot cm^{-2} \cdot min^{-1}$ at 650 °C and 0.53 $mL \cdot cm^{-2} \cdot min^{-1}$ at 750 °C have been achieved with an 0.8 mm thick BZY-MC membrane containing 52% porosity and 50%CO_2–N_2 feed gas. The high flux is attributed to synergistic effects of microstructure, MC loading and high bulk conductivity of BZY. In addition, we also demonstrate the positive effect of H_2O in the permeate side on CO_2 flux density and proposed a reasonable mechanism to explain the H_2O-enhanced CO_2 flux density. With 3% H_2O-added into the sweeping gas, the membrane exhibits 30% CO_2 flux density enhancement and good stability over 250 h at 650 °C.

Author's statement

Kangkang Zhang: performed experiments, data analysis and manuscript drafting. Shichen Sun: data analysis and manuscript drafting. Nansheng Xu: materials synthesis, performance testing. Kevin Huang: supervising, conceptualization and finalizing manuscript.

1. Introduction

In recent decades, global warming has significantly changed the world's climate, resulting in our daily life interruption, and economy loss [1]. Certain extreme weather such as floods and droughts has become more and more frequent in some regions. Credible evidence has confirmed that the emission of carbon dioxide (CO_2), a greenhouse gas, is a primary contributor to the global warming [2]. To deal with the global warming and climate change, several strategies have been proposed to abate CO_2 emissions: (1) increasing the use of clean energy (e.g., wind, solar, nuclear, etc.); (2) improving the conversion efficiency of energy (e.g., fuel cells and advanced turbines); and (3) implementing the carbon capture and storage (CCS) technology at major stationary emitting sources [3–5]. Among these options, CCS is currently considered the most practical solution to limit CO_2 emissions from existing power plants and stabilize atmospheric CO_2 concentration [6].

Nowadays, the state-of-the-art CO_2 capture technology at industrial scale mainly rely on reversible physical/chemical absorptions like post-combustion flue gas "amine absorption" [7,8]. However, this process is energy intensive and costly for large-scale commercial implementation [9]. In comparison to sorption-based technologies, conventional membrane-based technologies show reduced energy and cost, system modularity, and environmental-friendliness [10,11]. Since these membranes use porous polymer and inorganic materials, their permeability and selectivity suffer from the constraint of "Robeson Upper Bound" rule. In addition, their working temperature is limited to <200 °C, which is not suitable for capturing hot CO_2 and then directly converting it to valuable products at high temperatures [12–14]. Therefore, it is reasonable to develop high-temperature CO_2 transport membranes for combined CO_2 capture and conversion.

The first high-temperature CO_2 transport membrane was demonstrated by Lin and co-workers [15], consisting of CO_3^{2-} conducting phase (molten carbonate (MC) phase) and electron conducting phase (stainless steel, SS). However, the reaction between MC and SS causes stability issue. Later, Huang and co-workers replaced SS with Ag and solved the reaction problem; but Ag tends to sinter over long period of high-temperature operation [16]. In addition, this metal-MC membrane permeates both CO_2 and O_2, thus requiring a further separation of O_2 from CO_2 and restricting CO_2 separation from fuel gas mixtures [17]. In order to improve the membrane stability and capture CO_2 without O_2, a new dual-ion transport membrane consisting of an oxide-ion conducting phase and MC phase, viz., mixed oxide-ion and carbonate-ion conductor (MOCC), has been developed [18]. Fig. 1 shows the basic chemistry of

---

[*] Corresponding author.

E-mail address: huang46@cec.sc.edu (K. Huang).

https://doi.org/10.1016/j.memsci.2022.120421
Received 20 January 2022; Received in revised form 23 February 2022; Accepted 27 February 2022
Available online 4 March 2022

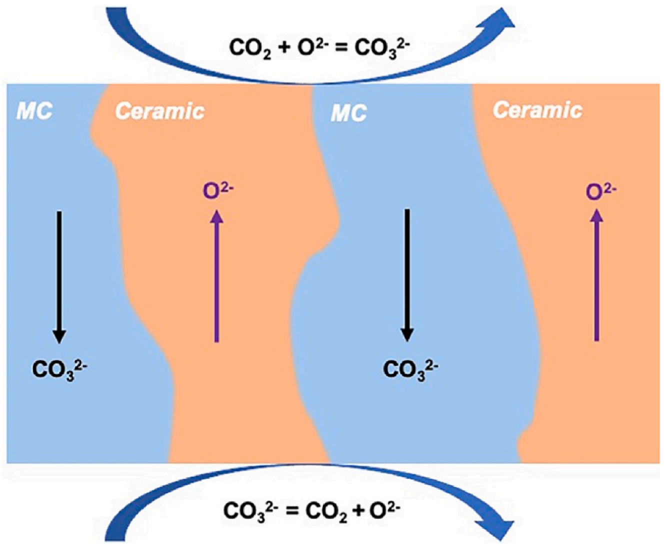

Fig. 1. Schematic of CO_2 separation chemistry across MOCC membrane.

CO_2 separation with a MOCC membrane. To enable CO_2 transport, CO_3^{2-} is formed by the reaction between CO_2 and O^{2-} (from the ceramic phase) on the feed (retentate, top) side of the membrane, and transported through the MC phase to the sweep (permeate, bottom) side, where pure CO_2 and O^{2-} are released to the sweeping gas and oxide-ion conducting phase, respectively. Notably, as a charge compensation to CO_3^{2-}, O^{2-} shares the same flux to CO_3^{2-} under steady state. The overall driving force for the CO_2 transport is the chemical potential gradient of CO_2 across the membrane.

Some early studies on MOCC membranes have been mainly reported on four types of oxide-ion conducting phases. Anderson and Lin [19] showed that a $La_{0.6}Sr_{0.4}Co_{0.8}Fe_{0.2}O_{3\text{-}\delta}$ (LSCF)-MC dual-phase membrane with a thickness of 0.375 mm achieved a flux of 0.35 mL · cm^{-2} · min^{-1} at 900 °C. Lu et al. [20] reported a thin yttria-stabilized zirconia (YSZ)-MC dual-phase membrane (~0.01 mm) with CO_2 flux density of 0.56 mL · cm^{-2} · min^{-1} at 650 °C. Rui et al. [21] reported a γ-Al_2O_3 modified $Bi_2Y_{0.3}Sm_{0.2}O_3$ (BYS)-MC dual-phase membrane of ~0.05 mm with a CO_2 flux of 0.083 mL · cm^{-2} · min^{-1} at 650 °C. One common problem with the above membranes is the poor long-term stability. Few years ago, our group first developed a MOCC based on samarium doped ceria (SDC) and achieved a high and stable 1.84 mL · cm^{-2} · min^{-1} at 700 °C even at a membrane thickness of 1.2 mm [22]. CeO_2-based MOCCs have since become the membrane of choice for high-flux and stable CO_2 separation from a variety of CO_2 sources [4].

In this work, we report for the first time a new dual-phase MOCC membrane comprising $BaZr_{0.8}Y_{0.2}O_{3\text{-}\delta}$ (BZY) and MC. The selection of BZY as the ceramic phase is based on the fact that it is known to be a mixed O^{2-} and H^+ conductor at intermediate-to-high temperatures upon exposure H_2O and excellent chemical stability in CO_2-containing atmospheres [23–25]. More importantly, the enhanced ionic conductivity in BZY by H_2O is cooperative with the positive effect of H_2O on CO_2 flux observed on MOCC membranes via the OH^- transport mechanism [26,27]. Given the fact that BZY can also conduct OH^- under wet conditions according to the following reaction [28] (using Kröger–Vink notation)

$$H_2O_{(g)} + V_O^{\cdot\cdot} + O_O^{\times} = 2(OH)_O^{\cdot} \tag{1}$$

where $V_O^{\cdot\cdot}$ and $O_O^{\times}$ represent oxygen vacancies and lattice oxygens, respectively; $(OH)_O^{\cdot}$ denotes protons residing on lattice oxygens. The presence of BZY phase in the MOCC dual-phase membrane is expected to increase OH^- concentration and provide additional pathways for OH^-, thus further improving the CO_2 permeation flux.

2. Experimental procedures

2.1. Preparation of BZY-MC dual-phase membrane

The BZY ($BaZr_{0.8}Y_{0.2}O_{3\text{-}\delta}$) was synthesized via conventional solid-state reaction. Stoichiometric amount of the starting materials ($BaCO_3$, ZrO_2, Y_2O_3 and NiO (1 wt% of product)) were ball-milled in alcohol with ZrO_2 balls for 6 h and dried at 80 °C overnight, followed by firing at 1000 °C for 6 h. The obtained powders were then blended with 5, 10, 20 wt% of carbon black as pore former, ball-milled for 6 h again. After mixing and drying, the powder mixture was pelletized under ~100 MPa and subsequently sintered at 1300 °C for 6 h. The resultant BZY pellets possess porous microstructure with a dimension of ~15 mm and 0.8 mm in thickness. The bare BZY-MC membranes were prepared by infiltrating *in situ* molten carbonate eutectic (Li_2CO_3:Na_2CO_3 = 52:48 mol%) into porous BZY matrix. The amount of MC addition into BZY matrix is determined by the pore volume fraction in the BZY matrix. To investigate the chemical compatibility between BZY and MC, we blended BZY with carbonate eutectic powders in 50:50 (wt%) ratio and fired at 750 °C for 2 h.

2.2. Characterization of porous BZY matrix and BZY-MC membrane

The phase structure of BZY was examined with X-ray diffraction (XRD, Rigaku D/MAX-2100 with Cu Kα radiation (λ = 1.5418 Å) from 10°-90°. Scanning electron microscope (SEM, Zessis Ultra plus) was applied to observe the microstructure of pure BZY pellets and BZY-MC dual phase membrane. Relative densities (ε) of the sintered porous BZY pellets were determined by the Archimedes' method. To extract other microstructural parameters of the porous matrix, *e.g.* tortuosity (τ) and average pore radius (r), we used helium permeation method as described in previous work [29]. Briefly, a porous BZY support was first sealed to a stainless-steel sample holder with silicone paste. The sample holder is then inserted into a chamber connected to a Helium cylinder and a mass flow controller. The downstream pressure (P_L) of the membrane is varied via the outlet valve, while the pressure difference through membrane (ΔP), the inlet pressure of the membrane (P_I) and the flow rate (f) are simultaneously recorded with a pressure differential sensor, pressure sensor and bubble flow meter, respectively.

The permeance of helium, F, through the porous matrix is calculated by

$$F = \left(\frac{Q}{S\cdot(P_I - P_L)}\right) \tag{2}$$

where S is the active area for permeating gas and Q is the molar flow rate of permeating helium calculated from the bubble flow meter (f).

According to the Darcy's law, F is given by [29].

$$F = \alpha + \beta\cdot\left(P_I - \frac{\Delta P}{2}\right) \tag{3}$$

where α and β are permeability coefficients related to Knudsen flow and viscous flow, respectively. The pore radius, r, is then given by

$$r = 8.4818\mu\sqrt{\frac{RT}{M_w}}\left(\frac{\beta}{\alpha}\right) \tag{4}$$

where R is the gas constant, T is absolute temperature, M_w is the molecular weight of helium. Since α and β are a function of ε/τ by the following equation

$$\alpha = 1.06\left(\frac{\varepsilon}{\tau}\right)\left(\frac{r}{L\sqrt{RTM_w}}\right) \tag{5}$$

$$\beta = 0.125\left(\frac{\varepsilon}{\tau}\right)\left(\frac{r^2}{L\mu RT}\right) \tag{6}$$

where L is the thickness of porous matrix and μ is the viscosity of helium, τ can be further calculated from the known τ and r values.

2.3. CO_2 flux measurement

The flux measurements were performed in a homemade permeation cell. The details can be found in our previous work [16]. The feed gas was a gas mixture of 25 mL min^{-1} CO_2 and 25 mL min^{-1} N_2, while a high-purity Ar at a flow of 50 mL min^{-1} was fed to the other side as the sweep gas. The presence of N_2 in feed gas was used to detect any physical leakage during test so that the CO_2 flux density can be corrected accordingly. The compositions of sweep gas were analyzed by an on-line GC (Agilent Micro 490-GC). The membrane was first heated to 550 °C at a rate of 2 °C/min and held for 1 h to ensure the MC fully melted and filled the matrix. Roughly 40 min were given at each testing temperature to ensure full equilibrium before collecting data. The flux densities of the CO_2 and N_2 were calculated by the following equation:

$$J_{CO_2} = \frac{C_{CO_2}}{1 - C_{CO_2} - C_{N_2}} \times \frac{Q}{S} \tag{7}$$

$$J_{N_2} = \frac{C_{N_2}}{1 - C_{CO_2} - C_{N_2}} \times \frac{Q}{S} \tag{8}$$

where Q is the mass flow rate of Ar sweeping gas; S is the effective area of the membrane, 0.921 cm^2 for this work; C_{CO_2} and C_{N_2} are the measured concentration of CO_2 and N_2 respectively.

To study the effect of H_2O partial pressure on the CO_2 flux, a range of steam contents (0–40%) was achieved by passing Ar through a homemade water saturator at different temperatures. The real steam content in the carrier gas, Ar, was measured by an on-line humidify sensors (Vaisala model 332).

3. Results and discussion

3.1. XRD analysis

Fig. 2 shows the XRD patterns of BZY sintered at different temperatures. The main perovskite phase in BZY is observed with impurity phase after calcination at 1000 °C for 6 h, which is due to incomplete reaction of precursors under this condition. A pure cubic perovskite BZY phase (corresponding to PDF#74–1299) is obtained after sintering at 1300 °C for 6 h.

In addition, the chemical stability between BZY and MC at high temperatures is also studied. Fig. 3 shows that for BZY-MC mixtures reacted at 650 °C and 750 °C, there is only a minor amount of $BaCO_3$ impurity phase observed. In contrast, a significant amount of $BaCO_3$ impurity phase is found after reacting at 850 °C, indicating that high temperature favors the chemical reaction between BZY and MC. These results suggest as long as the operating temperature is kept low enough, the reaction between BZY and MC is limited. Notably, the MC phase is not so obvious from the XRD pattern because of its amorphous nature.

3.2. Microstructural features

To obtain porous BZY matrices with different porosities, 5, 10, 20 wt % carbon black were evenly added to the BZY powders (denoted as BZY-5C, BZY-10C and BZY-20C, respectively) prior to final sintering at 1300 °C. The SEM images of Fig. 4a, c and 4e show increased porosity with carbon black content. It is also noticed that the pores are interconnected and distributed evenly across the matrix with an average pore size of ~500 nm. In order to further characterize the microstructure of porous BZY matrix, the porosity (ε) and tortuosity (τ) are measured as well; the results are listed in Table 1.

After impregnation with MC, Fig. 4b, d and 4f show that all pores in the porous BZY matrix are filled, resulting in a dense microstructure with intimate contact between MC and porous BZY skeleton, suggesting a good wettability between the two phases. Such a dense dual-phase microstructure ensures low physical leakage and increases the data reliability of the permeated CO_2 flux.

3.3. CO_2 permeation flux vs. temperature with dry sweeping gas

The temperature-dependent CO_2 flux densities measured from different membranes with 25 mL min^{-1} CO_2 and 25 mL min^{-1} N_2 as feed gas are shown in Fig. 5a. As expected, the CO_2 flux density improves with temperature for all samples, suggesting that CO_2 transport is a thermally activated process. At a given temperature, the CO_2 flux density also increases with the loading of MC phase, which can be attributed to synergistic effect of microstructure, MC loading and conductivity of each phase. At 650 °C, the level of CO_2 flux density increases from 0.27, 0.30 to 0.34 $mL \cdot cm^{-2} \cdot min^{-1}$ for BZY-5C through BZY-20C, respectively. The CO_2 flux density is also observed to follow closely Arrhenius relationship, see Fig. 5b, the slopes of which representing the activation energy, E_a, fall within the range of 0.35–0.40 eV. According to other studies [20,21], the limiting process of CO_2 transport in MOCC membranes is related to oxide-ion migration in the ceramic phase, thus E_a of

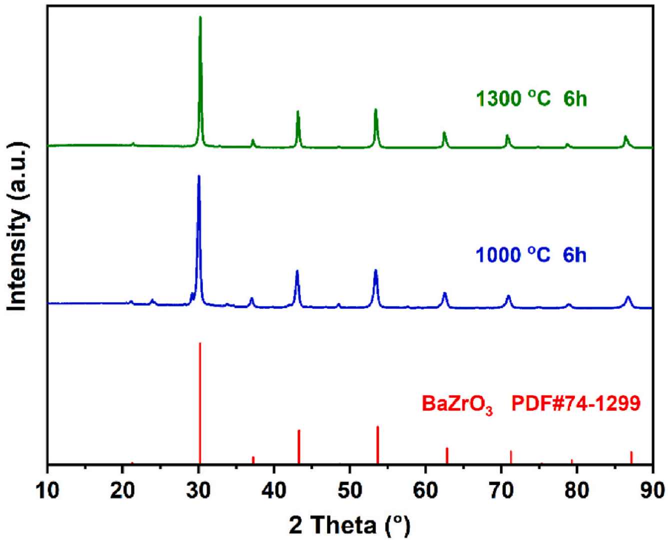

Fig. 2. XRD patterns of BZY calcined at 1000 °C and sintered at 1300 °C.

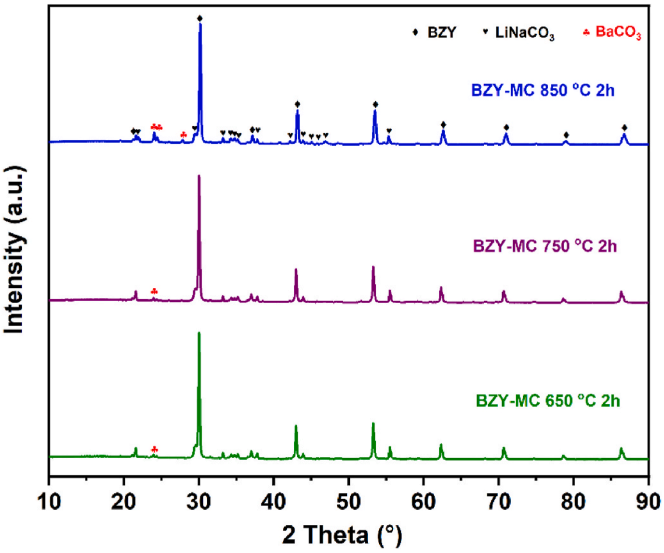

Fig. 3. XRD patterns of BZY-MC mixture reacted at 650, 750 and 850 °C.

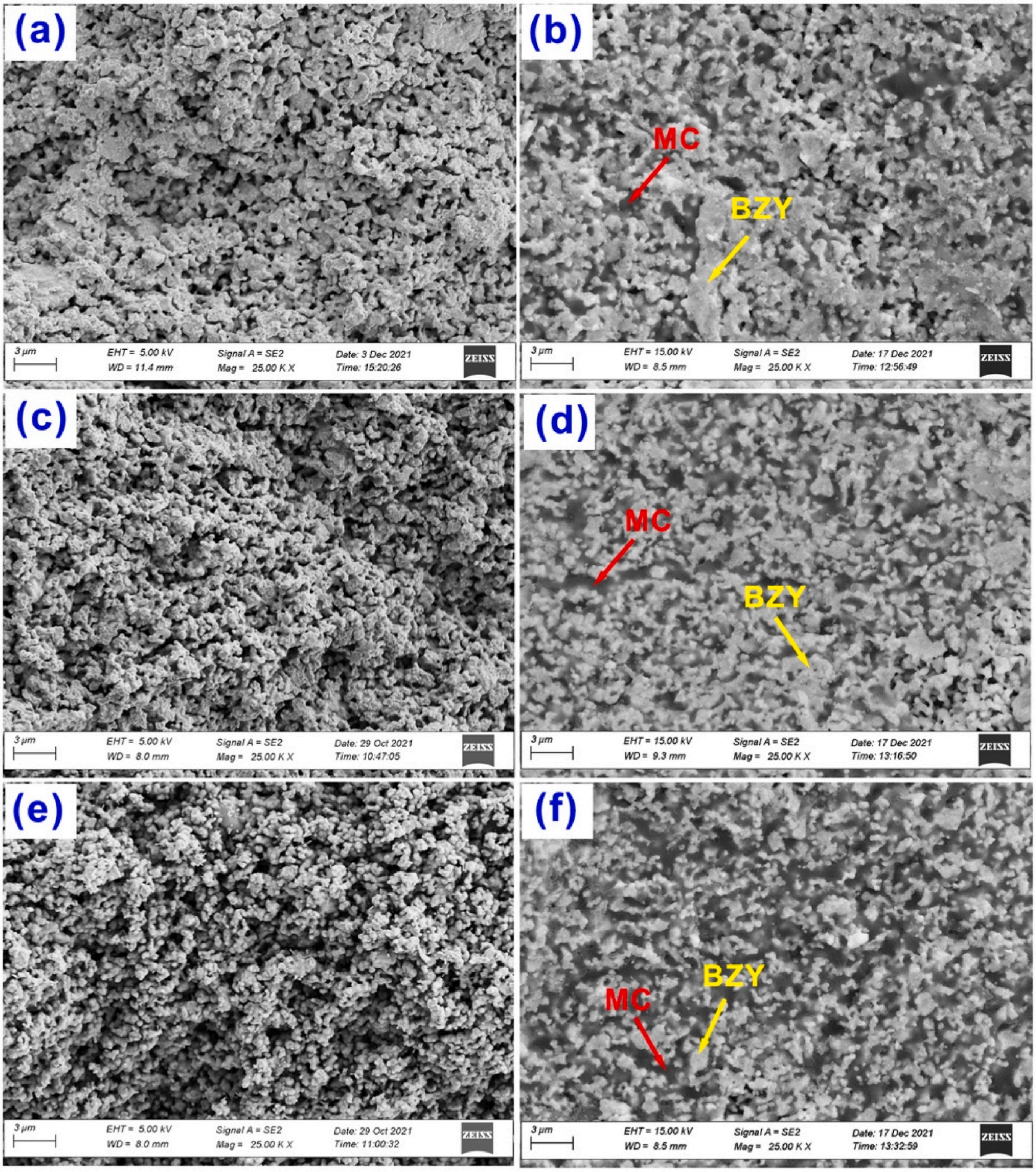

Fig. 4. Cross-sectional microstructure of the BZY porous matrix (a), (c), (e) and BZY-MC dual phase membranes (b), (d), (f) with 5, 10, 20 wt% carbon black addition respectively.

Table 1
Relative density and tortuosity of porous BZY-5C, 10C and 20C matrix, respectively.

Samples	ε	τ	*r* (*nm*)
BZY-5C	0.35	2.71	151
BZY-10C	0.45	2.34	193
BZY-20C	0.52	1.91	298

CO_2 transport in MOCC membrane should be close to that of oxide-ion conduction in the ceramic phase, which is in the range of 0.6–0.8 eV. However, the fact that total oxide-ion conductivity (including both grain and grain boundary) in BZY phase is as low as 10^{-5} S/cm at 700 °C [30] cannot explain the high flux density of BZY-MC membrane based on gas flux classical equation [31]. The observed high CO_2 flux density must have different mechanisms. Based on experimental and theoretical results [23,24], BZY possesses a very high bulk oxygen ion (O^{2-}) conductivity reaching 10^{-1} S/cm at 550–750 °C. We hypothesize that the presence of MC phase somehow eliminates the BZY grain-boundary effect. A piece of supporting evidence to this hypothesis is that E_a of CO_2 transport in BZY-MC membrane, see Fig. 4b, is surprisingly close to the theoretical $E_a = 0.42$ eV of O^{2-} migration in BZY bulk.

3.4. Theoretical CO_2 permeation flux vs. temperature

In order to validate our hypothesis, theoretical calculations were conducted. As the carbonate-ion conductivity is higher than oxide-ion conductivity in the BZY bulk phase, the CO_2 flux density can be

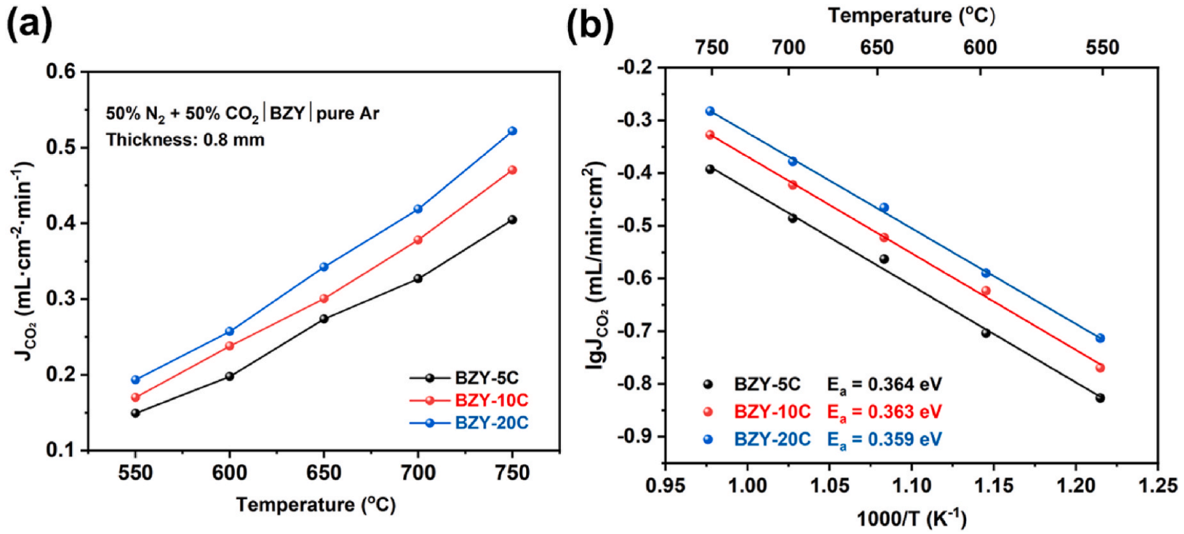

Fig. 5. Temperature dependence of CO_2 flux density of BZY-MC membranes with different carbon black addition (a) and corresponding Arrhenius plots (b).

described by the following equation:

$$J_{CO_2} = \frac{RT}{4nF^2}\frac{1}{L}\left(\frac{\varepsilon}{\tau}\right)\sigma_o\left[P'_{CO_2}{}^{n} - P''_{CO_2}{}^{n}\right] \quad (9)$$

where R is the ideal gas constant, 8.314 J mol^{-1} K^{-1}; T is absolute temperature, K; F is Faraday's constant, 96,500 C mol^{-1}; n is an empirical power index specific to the membrane; L is the membrane thickness, 0.08 cm in this work; ε and τ are the porosity and tortuosity for BZY matrix respectively, listed in Table 1; σ_o is the oxide-ion conductivity in the BZY bulk phase [23]; P'_{CO_2} and P''_{CO_2} are the partial pressures of CO_2 at the feed and sweep sides, respectively. The independently calculated values with n = 0.1 are shown and compared with the experimental data in Fig. 6. It is evident that the calculated CO_2 flux densities are in excellent agreement with those experimentally measured, validating the hypothesis that direct MC-facilitated O^{2-} transport within BZY bulk phase. We speculate that the value of n might be related to the defect equilibrium between BZY and MC phase, which is not very clear at the present time. Note that the slight deviation for BZY-20C-MC sample is noted at higher temperatures. The possible reason is that the higher MC loading in this sample promotes the reaction between BZY and MC at higher temperatures, further deteriorating CO_2 flux, thus leading to lower than calculated flux.

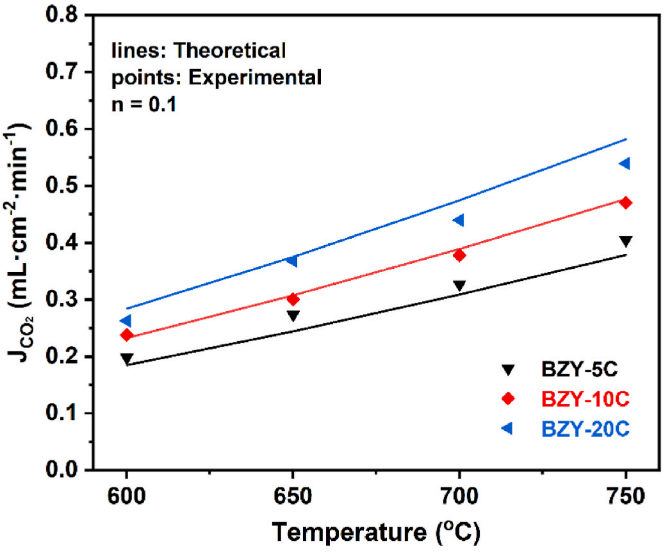

Fig. 6. Comparison of the measured CO_2 flux density with theoretical calculations.

3.5. CO_2 permeation flux vs. temperature with wet sweeping gas

The effect of H_2O addition into sweeping Ar on the CO_2 flux density (J_{CO_2}) was further investigated and the results are shown in Fig. 7a. With 3% H_2O addition, J_{CO_2} of all samples are enhanced. For example, CO_2 flux density of BZY-20C membrane reaches 0.45 and 0.60 mL · cm^{-2} · min^{-1} at 650 °C and 750 °C, respectively, which is 30% higher than that without H_2O addition, see Fig. 5a. Meanwhile, we also found that E_a of CO_2 permeation for all samples with 3% H_2O addition marginally decreased. For instance, it drops from 0.359 eV to 0.326 eV for BZY-20C-MC membrane before and after 3% H_2O addition, see Figs. 5b and 7b, respectively. It is worth mentioning that this H_2O enhancement on J_{CO_2} of MOCC could be significant as all flue gases contain ~10% steam.

To study the evolution of ceramic phase during testing, we performed SEM examinations on surfaces of both feed and sweep sides of the BZY-20C-MC membrane after it was tested in dry and wet sweep gas (Ar) at 650 °C. The images are shown in Fig. 8. First, the MC phase is seen well retained by the porous BZY matrix for both testing conditions, suggesting a good wettability between the BZY and MC. However, we did observe needle-like substance formed on both feed and sweep sides when the sweep-gas is moistened (Fig. 8c and d), whereas there is no such substance found when the sweep-gas is dry (Fig. 8a and b).

To further determine the composition of those needles, we performed a close-up SEM examination and elemental mapping on the feed-side surface (sweep side is expected to be the same because of H_2O presence in Ar sweep gas). The SEM image and mapping results are shown in Fig. 9. The results suggested that these needles are rich in Na and C, indicating that it could be Na_2CO_3 or $NaHCO_3$ phase. It could also contain Li_2CO_3 or $LiHCO_3$ phase, but the detection of Li and H is limited by the inability of energy-dispersive X-ray (EDX) spectroscopy to identify the lighter elements. We speculate that these needle phases are derived from the recrystallization of a molten phase (e.g. $(Li, Na)_2HCO_3$) during the cooling process.

To explain the H_2O-enhanced CO_2 flux, we propose the mechanisms in Fig. 10. Under dry sweeping gas conditions, see Fig. 10a, CO_3^{2-} formation can only take place at the gas/ceramic/MC triple-phase boundaries with O^{2-} in BZY phase as the only charge compensating species with respect to CO_3^{2-}. However, by introducing water to the sweep side, OH^- is formed as a product on the sweeping side of membrane via the following reaction:

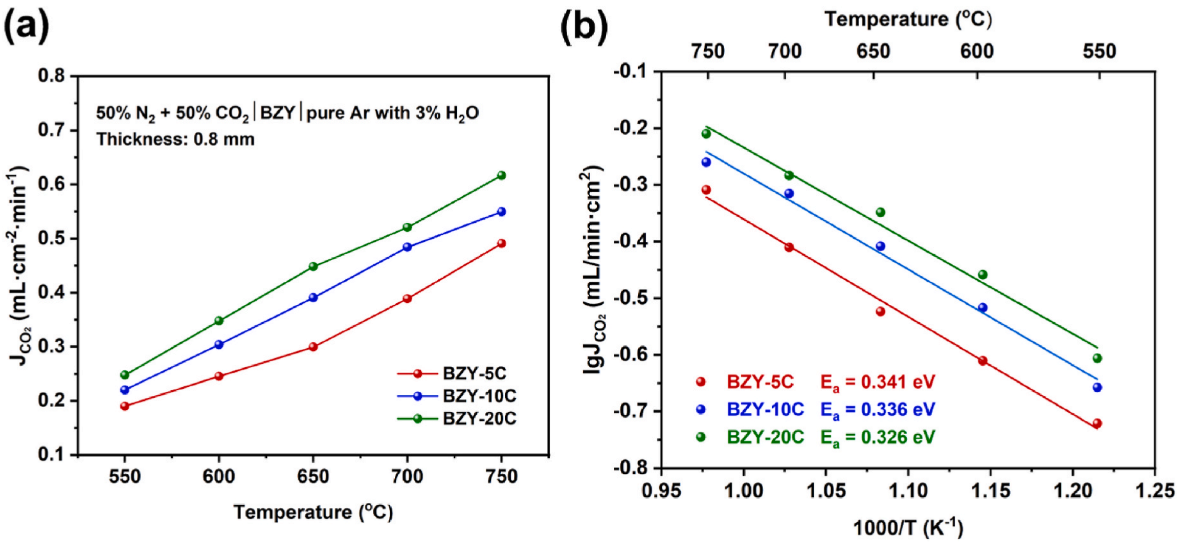

Fig. 7. Temperature dependence of CO_2 flux density of BZY-MC membranes with different carbon black addition under 3% H_2O-added Ar (a) and corresponding Arrhenius plots (b).

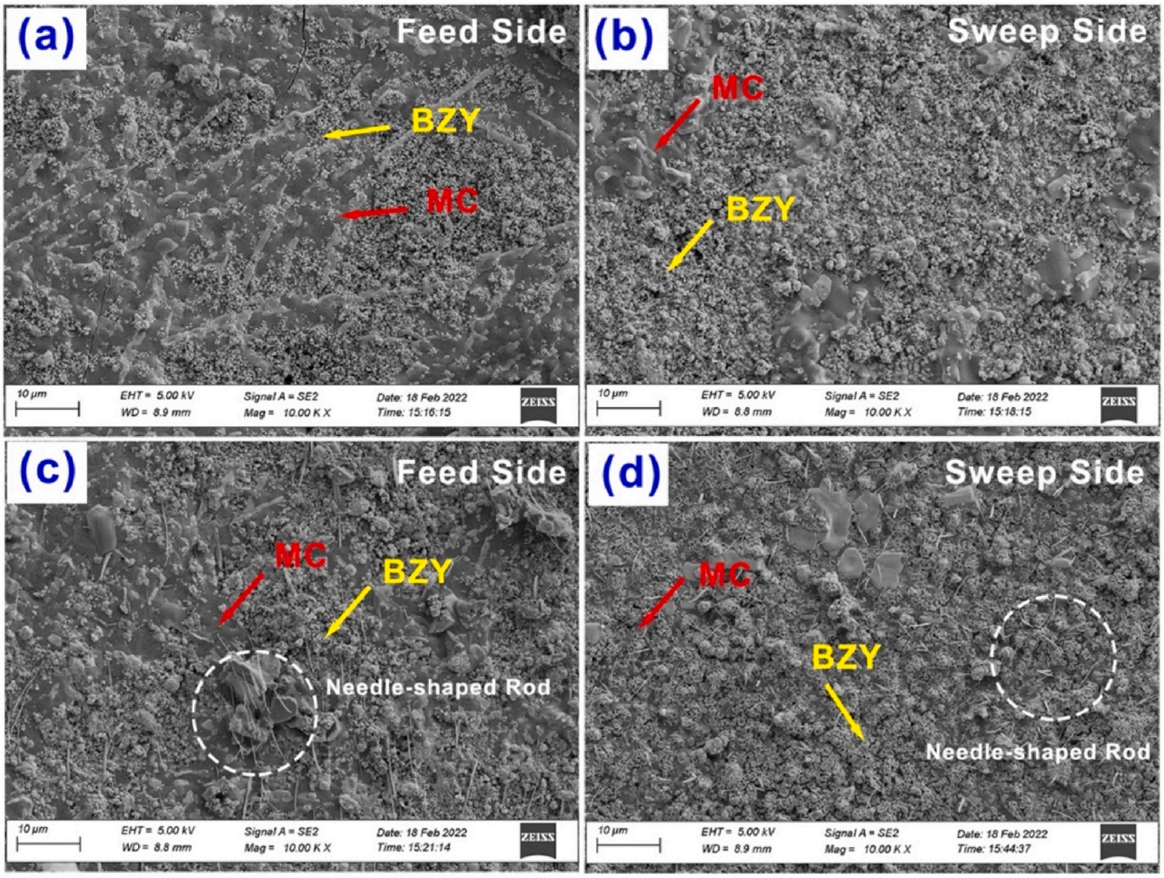

Fig. 8. Surface morphology of the post-test BZY-20C-MC membrane on the feed side (a), (c) and on the sweep side (b), (d) under dry Ar and 3% H_2O-added Ar condition, respectively.

$$H_2O + CO_3^{2-} = CO_2 + 2OH^- \tag{10}$$

Alternatively, reaction (10) can be viewed to proceed via the following two sub-steps:

$$H_2O + CO_3^{2-} = HCO_3^- + OH^- \tag{11}$$

$$HCO_3^- = CO_2 + OH^- \tag{12}$$

The generated OH^- is then transported through the MC phase toward the feed side via its chemical potential gradient. At the feed side surface, the following reverse reaction (overall) occurs:

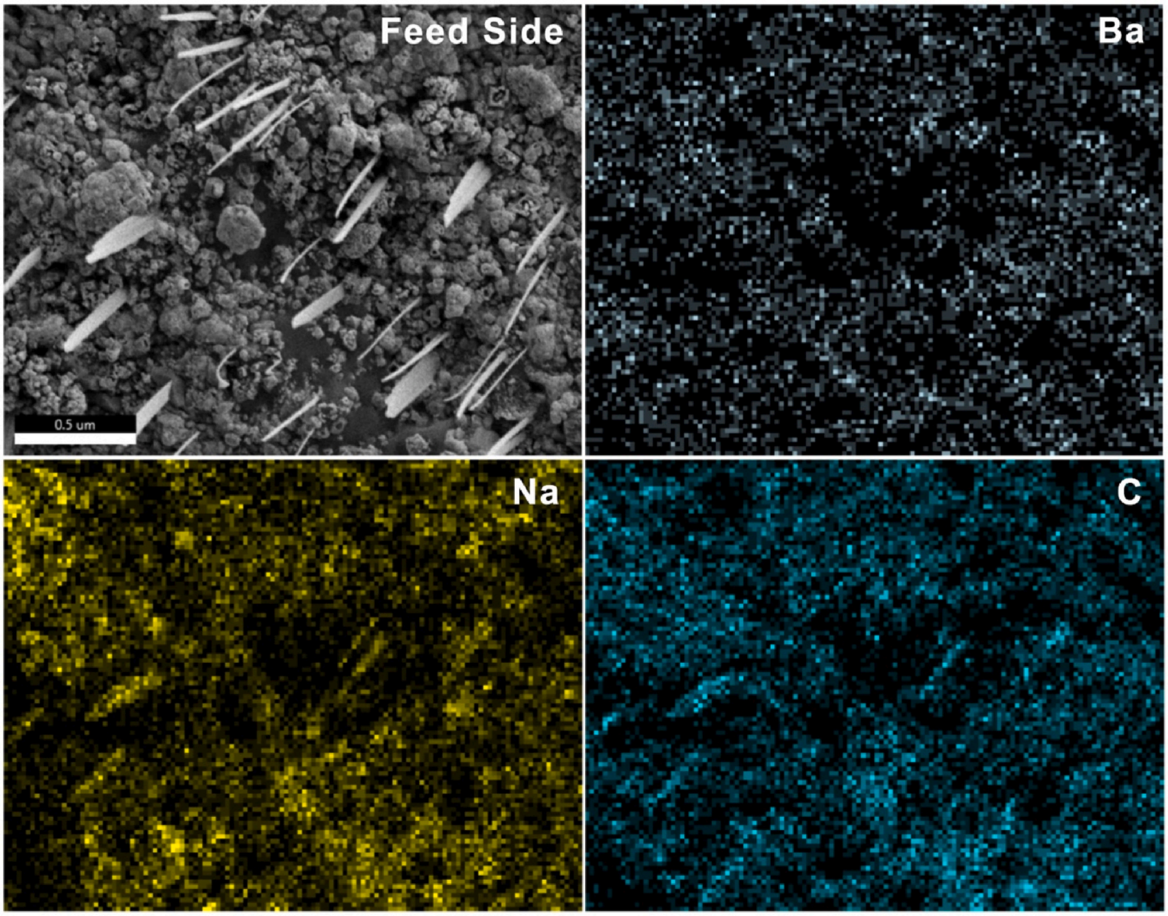

Fig. 9. Surface morphology and elemental mapping of post-tested BZY-20C-MC membrane on the feed side under 3% H_2O-added Ar condition.

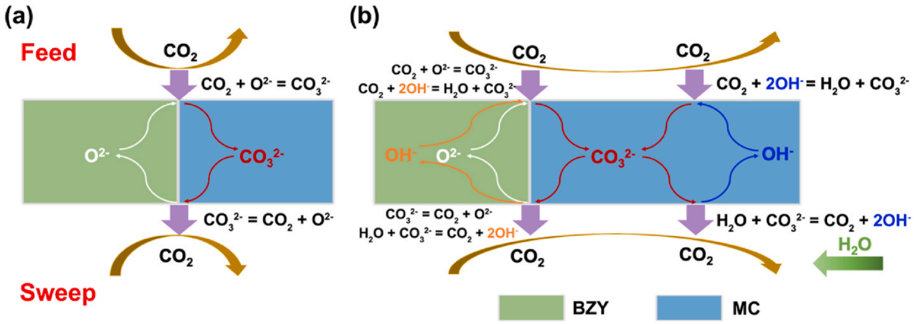

Fig. 10. Illustration of CO_2 transport mechanism in BZY-MC dual phase membrane under (a) dry and (b) wet sweeping gas condition.

$$CO_2 + 2OH^- = H_2O + CO_3^{2-} \tag{13}$$

The significant increase on J_{CO_2} can be understood by the presence of a new charge-compensating species (OH^-), which diffuses in the opposite direction in the MC phase, thus facilitating the overall ${CO_3}^{2-}$ transport by a new pathway created at the gas/MC two-phase boundaries and through the MC phase, see Fig. 10b. On the other hand, BZY is considered a good H^+ conductor with OH^- (H^+ residing on O^{2-} lattice) as the charge carrier. This reality provides an additional OH^- migration channel via BZY phase, which will further enhance the effect of H_2O on J_{CO_2}. It is expected that a higher J_{CO_2} can be achieved by further increasing H_2O partial pressure in the sweeping side.

3.6. *The effect of H_2O content on CO_2 permeation flux*

To further verify our proposed hypothesis, the CO_2 flux density of BZY-20C-MC membrane was studied as a function of P_{H_2O} in the sweeping side at 650 °C. In Fig. 11, a clear trend is observed, *i.e.* CO_2 flux increases with P_{H_2O}, as a result of additional OH^- pathway. A high $J_{CO_2} = 0.65$ mL$\cdot$ cm^{-2} $\cdot$ min^{-1} is achieved with 40% H_2O addition at 650 °C, while it returns to 0.45 mL $\cdot$ cm^{-2} $\cdot$ min^{-1} again after switching back to 3% H_2O, demonstrating the process is reversible.

To confirm water transport through the membrane, a humidity sensor was installed into feed gas line to analyze the H_2O content. The results are shown in Fig. 12. It is evident that there is H_2O presence in the feed gas; the more H_2O added to the sweep side, the more the H_2O on the feed side. The observation of H_2O on the feed side is a strong piece of

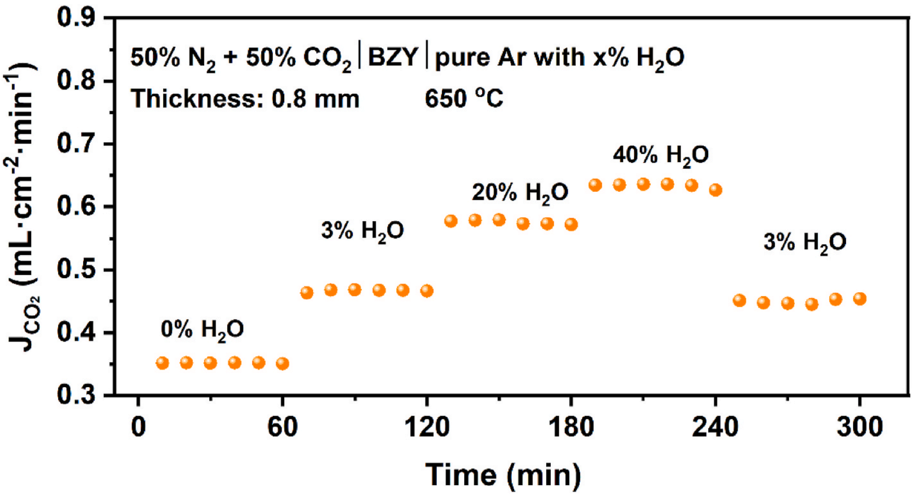

Fig. 11. CO_2 flux density of BZY-20C-MC membrane with different H_2O partial pressure in the sweeping side.

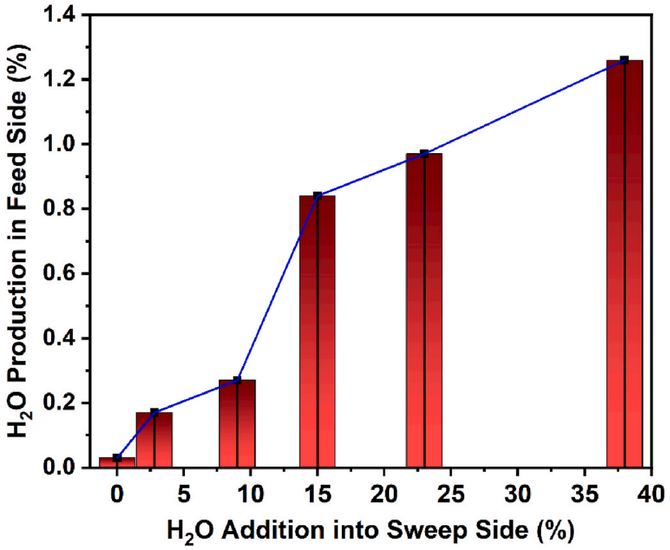

Fig. 12. The H_2O production in feed side under different H_2O addition into sweep side of BZY-20C-MC membrane at 650 °C.

supporting evidence for the mechanism proposed in Fig. 10. It is also interesting to note that H_2O content below 20% has the most significant impact on H_2O transport, above which the H_2O content in the feed gas appears to be flattened out. We believe that this is because the sweep-side surface becomes saturated by H_2O molecules at high H_2O content and a further increase in H_2O content would not improve H_2O transport too much. This surface limitation is also the reason why the increase of CO_2 flux density from 20 to 40% H_2O is not as significant as that from 0 to 20% H_2O (see Fig. 11).

3.7. *Long-term stability of CO_2 permeation flux*

The long-term stability of CO_2 flux density of BZY-20C-MC membrane was evaluated at 650 °C with 3%H_2O in Ar sweeping gas. Fig. 13a shows that the CO_2 flux reaches equilibrium after 1 h at 650 °C, and then remains stable at 0.45 $mL \cdot cm^{-2} \cdot min^{-1}$ for 250 h. We noted that there was a slight CO_2 flux fluctuation at 30 h but stabilizing itself after 20 h; this fluctuation might be related to an unintentional variation of H_2O change into sweep gas. In addition, the N_2 leakage is low (0.1 $mL \cdot cm^{-2} \cdot min^{-1}$) and remains relatively stable during the testing period, suggesting a good robustness of the membrane. XRD pattern of the post-long-term test sample shown in Fig. 13b did not reveal any additional impurity phase, indicating good chemical stability of BZY-20C-MC membrane under working condition.

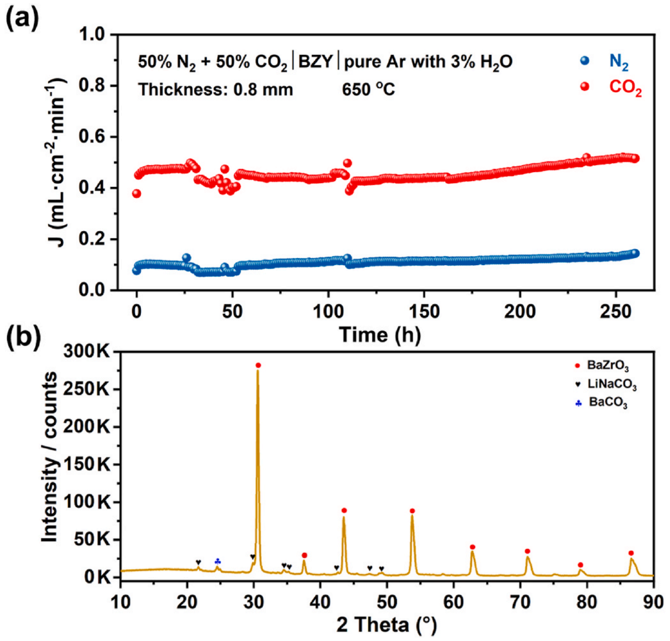

Fig. 13. (a) Long term stability of CO_2 flux density of BZY-20C-MC membrane with 3% H_2O into sweeping gas, (b) XRD pattern of the post-long-term test BZY-20C-MC membrane.

4. Conclusions

Ceramic-carbonate dual-phase MOCC membrane with a porous proton conducting $BaZr_{0.8}Y_{0.2}O_{3-\delta}$ (BZY) matrix and molten carbonate has been successfully synthesized in this study. Through the microstructural optimization, the permeated CO_2 flux of BZY-20C-MC membrane of 0.8 mm thickness is as high as 0.34 $mL \cdot cm^{-2} \cdot min^{-1}$ at 650 °C and 0.53 $mL \cdot cm^{-2} \cdot min^{-1}$ at 750 °C respectively. The high flux is thought to relate to the synergistic effect of modified microstructure, MC loading and high bulk oxide-ion conductivity of porous BZY matrix. The activation energy of CO_2 permeation of BZY-MC membranes is close to that of oxide-ion migration in the BZY bulk, suggesting the rate-limiting nature of oxide-ion conduction in BZY bulk for CO_2 transport in the BZY-

MC membrane. It is also demonstrated that introducing H_2O into the sweeping gas can significantly enhance CO_2 permeation, which can be ascribed to the formation of new charge balancing species (OH^-) in both of BZY and MC phases. With 3% H_2O addition, the BZY-20C-MC membrane exhibits a stable CO_2 permeation flux density of 0.45 $mL \cdot cm^{-2} \cdot min^{-1}$ over 250 h at 650 °C.

Declaration of competing interest

The authors declare that they have no known competing financial interests or personal relationships that could have appeared to influence the work reported in this paper.

Acknowledgments

This material is based upon work supported by the U.S. National Science Foundation under grant number CBET-1924095.

References

[1] G.A. Mutch, L. Qu, G. Triantafyllou, W. Xing, M.-L. Fontaine, I.S. Metcalfe, Supported molten-salt membranes for carbon dioxide permeation, J. Mater. Chem. 7 (2019) 12951–12973.

[2] J.C.M. Pires, F.G. Martins, M.C.M. Alvim-Ferraz, M. Simões, Recent developments on carbon capture and storage: an overview, Chem. Eng. Res. Des. 89 (2011) 1446–1460.

[3] I. Ganesh, Conversion of carbon dioxide into methanol – a potential liquid fuel: fundamental challenges and opportunities (a review), Renew. Sustain. Energy Rev. 31 (2014) 221–257.

[4] P. Zhang, J. Tong, K. Huang, X. Zhu, W. Yang, The current status of high temperature electrochemistry-based CO2 transport membranes and reactors for direct CO_2 capture and conversion, Prog. Energy Combust. Sci. 82 (2021) 100888.

[5] A.S. Agarwal, Y. Zhai, D. Hill, N. Sridhar, The electrochemical reduction of carbon dioxide to formate/formic acid: engineering and economic feasibility, ChemSusChem 4 (2011) 1301–1310.

[6] B. Smit, Carbon capture and storage: introductory lecture, Faraday Discuss 192 (2016) 9–25.

[7] V. R, I. Ss, S. Gk, B. Pg, A. S, W. Tk, Direct observation and quantification of CO2 binding within an amine-functionalized nanoporous solid, Science 330 (2010) 650–653.

[8] G.T. Rochelle, Amine scrubbing for CO2 capture, Science 325 (2009) 1652–1654.

[9] Mahmoud M. Abdelnaby, A.M. Alloush, N.A.A. Qasem, B.A. Al-Maythalony, R. B. Mansour, K.E. Cordova, O.C.S. Al Hamouz, Carbon dioxide capture in the presence of water by an amine-based crosslinked porous polymer, J. Mater. Chem. 6 (2018) 6455–6462.

[10] P. Zhang, J. Tong, K. Huang, A self-forming dual-phase membrane for high-temperature electrochemical CO2 capture, J. Mater. Chem. 5 (2017) 12769–12773.

[11] S. Zhao, P.H.M. Feron, L. Deng, E. Favre, E. Chabanon, S. Yan, J. Hou, V. Chen, H. Qi, Status and progress of membrane contactors in post-combustion carbon capture: a state-of-the-art review of new developments, J. Membr. Sci. 511 (2016) 180–206.

[12] T. Tomita, K. Nakayama, H. Sakai, Gas separation characteristics of DDR type zeolite membrane, Microporous Mesoporous Mater. 68 (2004) 71–75.

[13] J. Gilron, A. Soffer, Knudsen diffusion in microporous carbon membranes with molecular sieving character, J. Membr. Sci. 209 (2002) 339–352.

[14] K.M. Steel, W.J. Koros, An investigation of the effects of pyrolysis parameters on gas separation properties of carbon materials, Carbon 43 (2005) 1843–1856.

[15] J.H.P.S.J. Chung, D. Li, J.-I. Ida, I. Kumakiri, Jerry Y.S. Lin, Dual-phase metal-carbonate membrane for high-temperature carbon dioxide separation, Ind. Eng. Chem. Res. 44 (2005) 7999–8006.

[16] N. Xu, X. Li, M.A. Franks, H. Zhao, K. Huang, Silver-molten carbonate composite as a new high-flux membrane for electrochemical separation of CO_2 from flue gas, J. Membr. Sci. 401–402 (2012) 190–194.

[17] S. Zeng, Z. Liu, H. Zhao, T. Yang, X. Dong, Z. Du, A chemically stable La0.2Sr0.8Fe0.9Mo0.1O3-δ-molten carbonate dual-phase membrane for CO_2 separation, Separ. Purif. Technol. 280 (2022).

[18] J. Wade, K. Lackner, A. West, Transport model for a high temperature, mixed conducting CO_2 separation membrane, Solid State Ionics 178 (2007) 1530–1540.

[19] M. Anderson, Y.S. Lin, Carbonate–ceramic dual-phase membrane for carbon dioxide separation, J. Membr. Sci. 357 (2010) 122–129.

[20] B. Lu, Y.S. Lin, Synthesis and characterization of thin ceramic-carbonate dual-phase membranes for carbon dioxide separation, J. Membr. Sci. 444 (2013) 402–411.

[21] Z. Rui, M. Anderson, Y. Li, Y.S. Lin, Ionic conducting ceramic and carbonate dual phase membranes for carbon dioxide separation, J. Membr. Sci. 417–418 (2012) 174–182.

[22] L. Zhang, N. Xu, X. Li, S. Wang, K. Huang, W.H. Harris, W.K.S. Chiu, High CO_2 permeation flux enabled by highly interconnected three-dimensional ionic channels in selective CO2 separation membranes, Energy Environ. Sci. 5 (2012) 8310–8317.

[23] X. Li, L. Zhang, Z. Tang, M. Liu, Fast oxygen transport in bottlelike channels for Y-doped BaZrO3: a reactive molecular dynamics investigation, J. Phys. Chem. C 123 (2019) 25611–25617.

[24] D. Pergolesi, E. Fabbri, A. D'Epifanio, E. Di Bartolomeo, A. Tebano, S. Sanna, S. Licoccia, G. Balestrino, E. Traversa, High proton conduction in grain-boundary-free yttrium-doped barium zirconate films grown by pulsed laser deposition, Nat. Mater. 9 (2010) 846–852.

[25] Y. Liu, R. Ran, M.O. Tade, Z. Shao, Structure, sinterability, chemical stability and conductivity of proton-conducting $BaZr_{0.6}M_{0.2}Y_{0.2}O_{3-\delta}$ electrolyte membranes: the effect of the M dopant, J. Membr. Sci. 467 (2014) 100–108.

[26] W. Xing, T. Peters, M.-L. Fontaine, A. Evans, P.P. Henriksen, T. Norby, R. Bredesen, Steam-promoted CO_2 flux in dual-phase CO_2 separation membranes, J. Membr. Sci. 482 (2015) 115–119.

[27] S. Sun, Y. Wen, K. Huang, A new ceramic–carbonate dual-phase membrane for high-flux CO_2 capture, ACS Sustain. Chem. Eng. 9 (2021) 5454–5460.

[28] S. Imashuku, T. Uda, Y. Nose, G. Taniguchi, Y. Ito, Y. Awakura, Dependence of dopant cations on microstructure and proton conductivity of barium zirconate, J. Electrochem. Soc. 156 (2009) B1–B8.

[29] Y.S. Lin, A.J. Burggraafb, Experimental studies on pore size change of porous ceramic membranes after modification, J. Membr. Sci. 79 (1993) 65–82.

[30] A.S. Patnaik, A.V. Virkar, Transport properties of potassium-doped $BaZrO_3$ in oxygen- and water-vapor-containing atmospheres, J. Electrochem. Soc. 153 (2006) A1397–A1405.

[31] B. Lu, Y.S. Lin, Asymmetric thin samarium doped cerium oxide–carbonate dual-phase membrane for carbon dioxide separation, Ind. Eng. Chem. Res. 53 (2014) 13459–13466.